Editors' Suggestion

Evolution of structural, magnetic, and transport properties in $MnBi_{2-x}Sb_xTe_4$

J.-Q. Yan,[1,*] S. Okamoto,[1] M. A. McGuire,[1] A. F. May,[1] R. J. McQueeney,[2] and B. C. Sales[1]
[1]*Materials Science and Technology Division, Oak Ridge National Laboratory, Oak Ridge, Tennessee 37831, USA*
[2]*Ames Laboratory and Department of Physics and Astronomy, Iowa State University, Ames, Iowa 50011, USA*

(Received 2 July 2019; published 4 September 2019)

Here we report the evolution of structural, magnetic, and transport properties in $MnBi_{2-x}Sb_xTe_4$ ($0 \leqslant x \leqslant 2$) single crystals. $MnSb_2Te_4$, isostructural to $MnBi_2Te_4$, is successfully synthesized in single-crystal form. Magnetic measurements suggest an antiferromagnetic order below $T_N = 19$ K for $MnSb_2Te_4$ with the magnetic moments aligned along the crystallographic c axis. With increasing Sb content in $MnBi_{2-x}Sb_xTe_4$, the a-lattice parameter decreases linearly following Vegard's law, while the c-lattice parameter shows little compositional dependence. The contraction along a is caused by the reduction of the Mn-Te-Mn bond angle, while the Mn-Te bond length remains nearly constant. The antiferromagnetic ordering temperature slightly decreases from 24 K for $MnBi_2Te_4$ to 19 K for $MnSb_2Te_4$. More dramatic change was observed for the critical magnetic fields required for the spin-flop transition and the moment saturation. Both critical fields decrease with increasing Sb content for $x \leqslant 1.72$; a spin-flip transition occurs in $MnSb_2Te_4$ at a small field of 3 kOe applied along the c axis. In high magnetic fields, the saturation moment at 2 K shows significant suppression from 3.56 μ_B/Mn for $MnBi_2Te_4$ to 1.57 μ_B/Mn for $MnSb_2Te_4$. Analysis of the magnetization data suggests that both the interlayer magnetic interaction and single-ion anisotropy decrease with increasing Sb content for $x \leqslant 1.72$. The partial substitution of Bi by Sb also dramatically affects the transport properties. A crossover from n-type to p-type conducting behavior is observed around $x \approx 0.63$. Our results show close correlation between structural, magnetic, and transport properties in $MnBi_{2-x}Sb_xTe_4$ and that partial substitution of Bi by Sb is an effective approach to fine tuning both the magnetism and transport properties of $MnBi_{2-x}Sb_xTe_4$.

DOI: 10.1103/PhysRevB.100.104409

I. INTRODUCTION

Intrinsic magnetic topological insulators are ideal for realizing exotic quantum states of matter such as an axion insulator and the quantum anomalous Hall effect at elevated temperatures. It has recently been proposed that $MnBi_2Te_4$ is the first example of an antiferromagnetic topological insulator [1,2], which has immediately triggered extensive theoretical and experimental studies on bulk, thin films, and thin flakes [3–11]. As shown in the inset of Fig. 1(a), the rhombohedral crystal structure of $MnBi_2Te_4$ can be viewed as inserting one Mn-Te layer into the quintuple layers of Te-Bi-Te-Bi-Te in Bi_2Te_3 [12]. The antiferromagnetic order below 24 K of the Mn sublattice has been studied theoretically and experimentally [2,13,14]. Mn^{2+} ions adopt a high-spin $S = 5/2$ and order into an A-type antiferromagnetic structure with ferromagnetic layers coupled antiferromagnetically along the c axis. An ordered moment of 4.04(13) μ_B/Mn at 10 K was found to align along the c axis by neutron diffraction [14]. $MnBi_2Te_4$ is thus a unique natural heterostructure of magnetic layers intergrowing with layers of a topological insulator. It is worth mentioning that $MnBi_2Te_4$ inherits the van der Waals bonding between the quintuple layers in Bi_2Te_3. This feature facilitates the investigation of quantum phenomena in $MnBi_2Te_4$ flakes with reduced/controlled thickness employing the exfoliation techniques developed for two-dimensional materials. This is well illustrated by the recent observation of a field-induced quantized anomalous Hall effect [11] and quantum phase transition from axion insulator to Chern insulator in $MnBi_2Te_4$ flakes [15].

The as-grown $MnBi_2Te_4$ single crystals are heavily electron doped, possibly due to nonstoichiometry or antisite defects [2,6,10,14,16]. A fine tuning of the Fermi level is needed to realize the proposed topological properties. This approach is taken in Cr-doped $Bi_{2-x}Sb_xTe_3$, where Chang *et al.* observed the quantum anomalous Hall effect: The randomly distributed Cr provides the ferromagnetism and Sb substitution fine tunes the charge carrier concentration and mobility [17]. Since Mn ions occupy a specific crystallographic site in the layered $MnBi_2Te_4$, intuitively we would expect that the Mn-Te layers and Bi-Te layers can be tuned independently with chemical substitutions targeted for different crystallographic sites to optimize the magnetism and electronic band structure separately. However, the magnetism and transport properties can be intimately coupled and the fine tuning of one property might have a dramatic effect on the other.

In this work, we report a thorough study of the evolution of structural, magnetic, and electrical properties in $MnBi_{2-x}Sb_xTe_4$. We also report the successful synthesis and physical properties of $MnSb_2Te_4$, which has been proposed [13] to be isostructural to $MnBi_2Te_4$ but has not been experimentally investigated. The existence of $MnSb_2Te_4$ makes it possible to synthesize a complete solid solution $MnBi_{2-x}Sb_xTe_4$. X-ray powder diffraction data reveal the same rhombohedral structure (space group R-3m) in the

*yanj@ornl.gov

 ©2019 American Physical Society

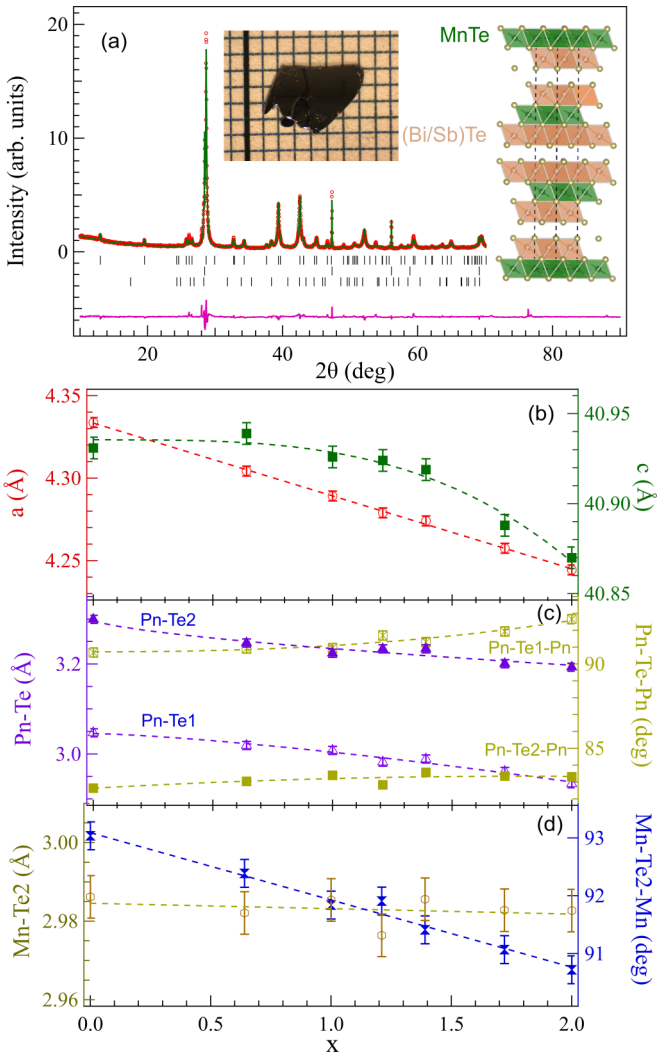

FIG. 1. Results of room-temperature x-ray powder diffraction. (a) Rietveld fit of powder x-ray diffraction data collected from $MnSb_2Te_4$ crystals ground with fine silicon powder. The upper, middle, and lower tick marks locate reflections from $MnSb_2Te_4$, silicon, and Sb_2Te_3, respectively. The inset shows the picture of one $MnSb_2Te_4$ single crystal on a millimeter grid and illustrates the crystal structure for the whole series of $MnBi_{2-x}Sb_xTe_4$. (b)–(d) Doping dependence of (b) lattice parameters, (c) Pn-Te bond length and Pn-Te-Pn bond angle (Pn=pnictogen), and (d) Mn-Te bond length and Mn-Te-Mn bond angle. The dashed curves are a guide to the eye.

whole composition range. The partial substitution of Bi by Sb is expected to tune the Fermi level without disturbing the magnetic layers. Indeed, we observed dramatic doping effects on the transport properties. A crossover from *n*-type to *p*-type conducting behavior is observed around $x \approx 0.63$. However, we also observed dramatic doping effects on the structural and magnetic properties, suggesting intimate coupling of the structural, magnetic, and electrical properties in $MnBi_{2-x}Sb_xTe_4$. With increasing Sb content, the lattice parameters, the antiferromagnetic ordering temperature, Weiss constant, saturation moment, and the critical fields for the spin flop transition and moment saturation all decrease. Analysis of the magnetization data suggests that both the interlayer magnetic interaction and single-ion anisotropy decrease with increasing Sb content for $x \leqslant 1.72$.

II. EXPERIMENTAL DETAILS

$MnBi_{2-x}Sb_xTe_4$ single crystals were grown out of a Bi(Sb)-Te flux [14]. The stoichiometry of each composition was determined by elemental analysis on a cleaved surface using a Hitachi TM-3000 tabletop electron microscope equipped with a Bruker Quantax 70 energy-dispersive x-ray system. At least two pieces of crystals from each batch were checked. We did not observe any compositional variation for crystals from the same batch or for the same piece of crystal but at different positions. The experimentally determined composition is used in the manuscript. All crystals are platelike with a typical in-plane dimension of 3 × 4 mm and a thickness in the range of 0.1–1 mm depending on the growth time. The single crystals are soft and can be easily exfoliated, which makes it difficult to collect high-quality single-crystal x-ray diffraction data. We thus gently ground the single crystals together with a fine powder of silicon and then performed x-ray powder diffraction at room temperature using a PANalytical XPert Pro diffractometer with Cu-$K_{\alpha 1}$ radiation. The fine silicon powder helps to grind the soft crystals without inducing severe strain [18].

Magnetic properties were measured with a Quantum Design (QD) Magnetic Property Measurement System in the temperature range $2.0 \leqslant T \leqslant 300$ K and in applied magnetic fields up to 70 kOe. Magnetization in magnetic fields up to 120 kOe was measured using the AC Measurement System (ACMS) option of a 14 T QD Physical Property Measurement System (PPMS). The temperature- and field-dependent electrical resistivity data were collected using a 9 T QD PPMS.

To gain insights into the electronic structure of $MnBi_{2-x}Sb_xTe_4$, we carried out density functional theory (DFT) calculations. We used the Vienna *ab initio* simulation package (VASP) [19] with the projector augmented wave method [20] and the generalized gradient approximation in the parametrization of Perdew, Burke, and Ernzerhof [21] for exchange correlation. We do not include $+U$ corrections because these compounds are itinerant semiconductors with strong hybridization between Mn 3*d* states and Te 5*p* states. For Te and Sb, we use the standard potential in the VASP distribution. For Bi (Mn), we use the potential in which the low-lying *d* (semi core *p*) states are treated as valence states, Bi_d (Mn_{pv}). To accommodate the antiferromagnetic ordering, we double the experimental structural unit cell along the *c* axis and then use a 12 × 12 × 2 **k**-point grid with an energy cutoff of 500 eV. The relativistic spin-orbit coupling is turned on, which allows us to analyze the single-ion spin anisotropy in addition to the magnetic coupling. To avoid the complexity arising from the random distribution of Bi and Sb at $0 < x < 2$, we only consider two end compounds, $MnBi_2Te_4$ ($x = 0$) and $MnSb_2Te_4$ ($x = 2$).

III. RESULTS

A. Structural properties

X-ray diffraction from cleaved surfaces of all compositions shows the same series of sharp *(00l)* reflections, which suggests that all investigated compositions have the same

TABLE I. The structure parameters of $MnBi_{2-x}Sb_xTe_4$ obtained from room-temperature x-ray powder diffraction patterns. The space group is *R*-3*m* (no. 166). Atomic coordinates are Mn (0, 0, 0), Bi (0, 0, *z*), Te1 (0, 0, *z*), and Te2 (0, 0, *z*).

x	0	0.63	1.0	1.39	2
a (Å)	4.3338(4)	4.3043(4)	4.2892(5)	4.2741(4)	4.2445(3)
c (Å)	40.931(6)	40.939(5)	40.926(6)	40.918(5)	40.870(5)
*z*_Bi(Sb)	0.4250(6)	0.4246(6)	0.4245(6)	0.4245(6)	0.4250(6)
*z*_Te1	0.1342(4)	0.1332(4)	0.1329(4)	0.1323(4)	0.1312(4)
*z*_Te2	0.2935(8)	0.2931(8)	0.2926(8)	0.2923(8)	0.2917(8)
χ^2	6.58	3.63	3.35	2.41	3.86

structure. This is further confirmed by the x-ray powder diffraction measurements performed on crystals gently ground with fine silicon powder. Our x-ray diffraction measurements do not suggest any ordering of Bi and Sb in the doped compositions or the formation of other $MnB_{2n}Te_{3n+1}$ (*B*=Bi or Sb or mixture) phases with $n > 1$ [22]. Reitveld refinement suggests 3–5%wt of $Bi_{2-x}Sb_xTe_3$ in the ground crystal, which likely comes from the residual flux on the crystal surface. As reported before [14], ferromagnetic Mn-doped $Bi_{2-x}Sb_xTe_3$ might affect the magnetic susceptibility at low fields.

Figure 1 shows the diffraction pattern of $MnSb_2Te_4$ and a Reitveld refinement as an example. The results of the Reitveld fit of some selected compositions are summarized in Table I. With increasing Sb content, the *a*-lattice parameter decreases, following Vegard's law. The *c*-lattice parameter of $MnSb_2Te_4$ is slightly smaller than that of $MnBi_2Te_4$. While the Mn-Te bond length shows little change with doping, the Mn-Te-Mn bond angle decreases linearly from 93 deg for $MnBi_2Te_4$ to 90.75 deg for $MnSb_2Te_4$. Both Pn-Te1 (Pn=pnictogen) and Pn-Te2 bonds contract with increasing Sb content. The Pn-Te2-Pn bond angle shows little compositional dependence. In contrast, the Pn-Te1-Pn bond angle increases gradually with doping from 90.8 deg for $MnBi_2Te_4$ to 92.6 deg for $MnSb_2Te_4$. The doping-induced change in nearest-neighbor Mn-Mn distance, i.e., the *a*-lattice parameter, and Mn-Te-Mn bond angle might be of particular importance in understanding the in-plane magnetic interactions.

B. Magnetic properties

Fifteen compositions of $MnBi_{2-x}Sb_xTe_4$ with different Bi/Sb ratios were studied. Figures 2(a)–2(e) show the temperature dependence of the magnetic susceptibility below 40 K of some selected compositions. The data were collected in a magnetic field of 1 kOe applied perpendicular and parallel to the crystallographic *c* axis. All measurements were done in a field-cooling mode. The data for $x = 0$ are replotted from our previous report [14].

The magnetic susceptibility is anisotropic below about 30 K. For $MnSb_2Te_4$, a cusp in the M/H curve was observed around 19 K when the magnetic field is applied along the crystallographic *c* axis, suggesting the occurrence of a long-range magnetic order. The anisotropic behavior of M/H below 19 K suggests an antiferromagnetic order with moments along the *c* axis as that found in $MnBi_2Te_4$. With increasing Sb content in

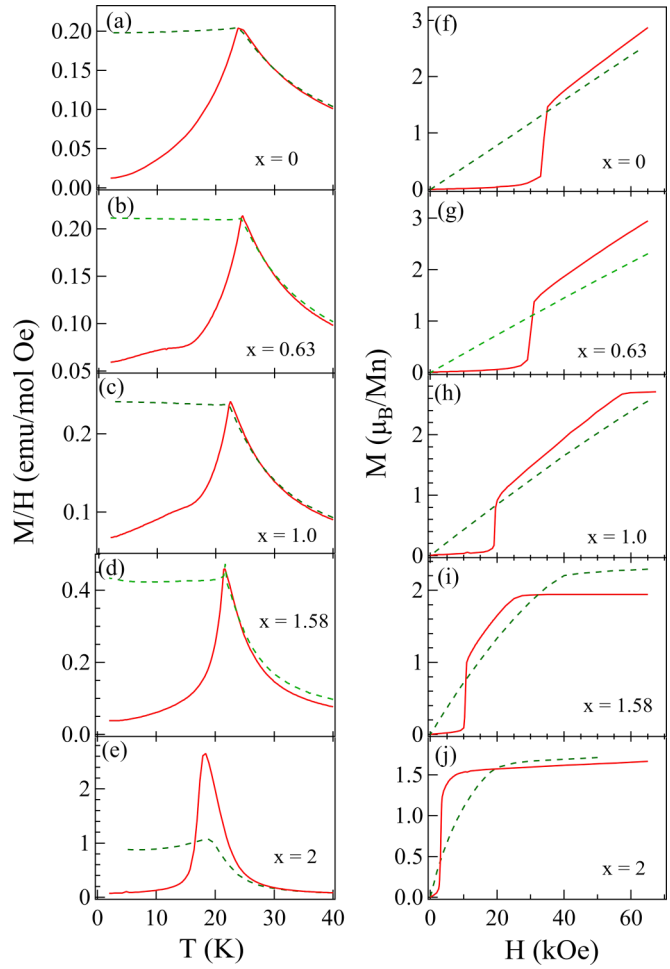

FIG. 2. (a)–(e) Temperature dependence of magnetic susceptibility, M/H, of selected compositions measured in a field of 1 kOe applied parallel ($H//c$, solid curve) and perpendicular ($H//ab$, dashed curve) to the crystallographic *c* axis, respectively. The weak feature around 12 K in the solid curves in (b) and (c) comes from the ferromagnetic impurity [14]. (f)–(j) Field dependence of magnetization of selected compositions measured at 2 K in fields up to 70 kOe applied parallel ($H//c$, solid curve) and perpendicular ($H//ab$, dashed curve) to the crystallographic *c* axis, respectively. Note that the demagnetization correction is not performed for data with $H//c$ because a demagnetization factor $n = 1$ has a negligible effect on the *MH* curves.

$MnBi_{2-x}Sb_xTe_4$, the antiferromagnetic ordering temperature, T_N, gradually decreases from 24 K for $MnBi_2Te_4$ to 19 K for $MnSb_2Te_4$. It is worth mentioning that the magnitude of M/H below T_N increases with Sb concentration. This is consistent with the fact that the fields required to flop the spins and saturate the moments decrease with increasing Sb doping, as described below. Despite the large difference of M/H below ≈30 K, all compositions have a magnetic susceptibility of around 1.0×10^{-3} emu/mol Oe at room temperature.

Figures 2(f)–2(j) show the field dependence of magnetization, $M(H)$, at 2 K in magnetic fields up to 70 kOe. The isothermal magnetization curves at 2 K for $x = 0$ and 0.63 were also measured in fields up to 120 kOe using a QD PPMS (see Fig. 7). For all compositions with $x \leqslant 1.72$,

a spin-flop transition can be well resolved in $M(H)$ curves when the magnetic field is applied along the c axis. The magnetic field required for the spin-flop transition decreases with increasing Sb content, from 33 kOe for $MnBi_2Te_4$ to 10 kOe for $MnBi_{0.28}Sb_{1.72}Te_4$. Meanwhile, the magnetic field required to saturate the moments also decreases with increasing Sb content, from 78 kOe for $MnBi_2Te_4$ to 22 kOe for $MnBi_{0.28}Sb_{1.72}Te_4$ for $H//c$. When the magnetic field is applied perpendicular to the c axis, the magnetization saturates at higher fields and the field required to saturate the moments also decreases with increasing Sb content from 103 kOe for $MnBi_2Te_4$ to 37 kOe for $MnBi_{0.28}Sb_{1.72}Te_4$. For $MnSb_2Te_4$, only a spin-flip transition occurs at 3 kOe for $H//c$. For $H//ab$, the magnetization saturates at 20 kOe. We notice that the saturation moment drops dramatically with increasing Sb doping from 3.56 μ_B/Mn for $MnBi_2Te_4$ to 1.57 μ_B/Mn for $MnSb_2Te_4$.

Figure 3 shows the inverse magnetic susceptibility, H/M, for three compositions. Only the data collected with $H//ab$ were shown because no anisotropic behavior was observed above 30 K. H/M curves show a linear temperature dependence above 80 K for all compositions. For $MnBi_2Te_4$, the linear temperature dependence extends to $T_N = 24$ K. However, with the partial substitution of Bi by Sb, H/M curves near T_N deviate from the high-temperature linear temperature dependence. As shown in Fig. 3, the deviation occurs around 80 K for $MnSb_2Te_4$. This suggests that Sb doping induces short-range magnetic correlations above T_N and up to 80 K for $MnSb_2Te_4$. The short-range magnetic correlations in the paramagnetic state affect the transport properties in this temperature range, as presented later. The Curie-Weiss fitting of the data in between 100 and 300 K shows that the effective moment is around 5.30 μ_B/Mn for all compositions without noticeable compositional dependence. However, the Weiss constant gradually changes from 6 K for $MnBi_2Te_4$ to -19 K for $MnSb_2Te_4$. This suggests that the dominant magnetic interaction is changed from ferromagnetic to antiferromagnetic with increasing Sb content, indicating complex competing interactions in $MnBi_{2-x}Sb_xTe_4$ which deserves detailed studies using techniques such as inelastic neutron scattering. The doping dependence of the Weiss constant is summarized in Fig. 9, presented later.

The Sb doping induces significant changes in the magnetic properties as well as interlayer coupling and single-ion anisotropy, as discussed later. The anisotropic magnetic properties suggest an antiferromagnetic order with moments along the c axis in $MnBi_{2-x}Sb_xTe_4$. All compositions might maintain the same A-type antiferromagnetic order as in $MnBi_2Te_4$, yet this needs further confirmation from other measurements such as neutron diffraction. The greatly suppressed saturation moment in $MnSb_2Te_4$ might signal strong magnetic fluctuations below T_N or complex spin arrangement in the ab plane in the presence of high magnetic fields.

C. Transport properties

The temperature and field dependence of in-plane electrical resistivity were measured in the temperature range $2 \leqslant T \leqslant 300$ K and in magnetic fields up to 90 kOe with the electrical current in the ab plane and the field along the c axis. Figure 4 shows the temperature dependence of in-plane electrical resistivity, $\rho(T)$, of some selected compositions. Above about 50 K, the $\rho(T)$ curves for all compositions show a positive temperature dependence. While ρ(300 K) of most compositions is around 1.2 mΩ cm, ρ(300 K) has a value of $\approx$3.0 mΩ cm around $x\approx$0.63 where the crossover from n-type to p-type conducting behavior occurs. The compositional-dependent transport properties require an understanding of changes in carrier type/concentration, chemical disorder effects, and coupling to the structure and magnetism.

As highlighted in the inset of Fig. 4, $\rho(T)$ of $MnBi_2Te_4$ and $MnSb_2Te_4$ shows quite different temperature-dependence cooling across T_N. $\rho(T)$ of $MnBi_2Te_4$ shows a cusp

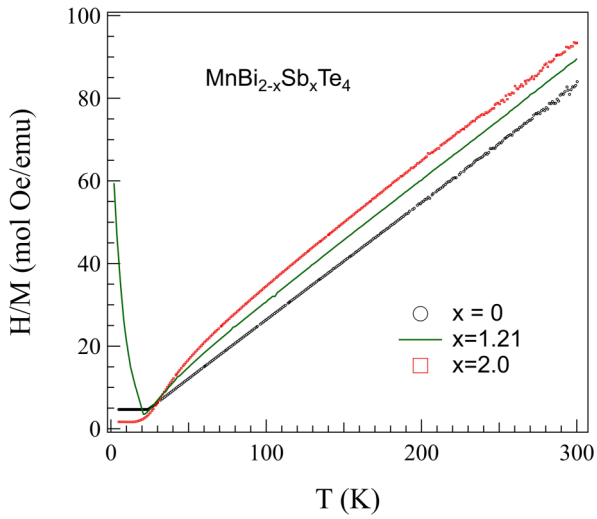

FIG. 3. Temperature dependence of reciprocal magnetic susceptibility, H/M, of selected compositions measured in a field of 10 kOe applied perpendicular ($H//ab$) to the crystallographic c axis.

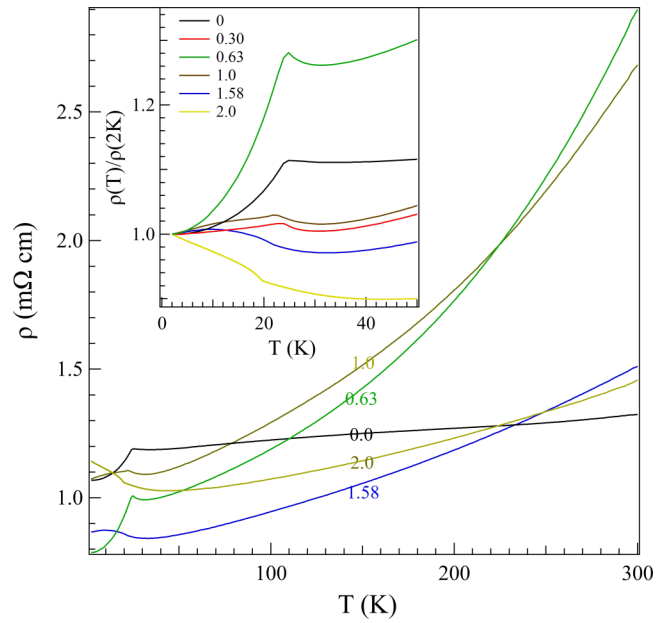

FIG. 4. The temperature dependence of in-plane electrical resistivity. The inset shows the normalized in-plane electrical resistivity, $\rho(T)/\rho(2\text{ K})$ to highlight the features at low temperatures.

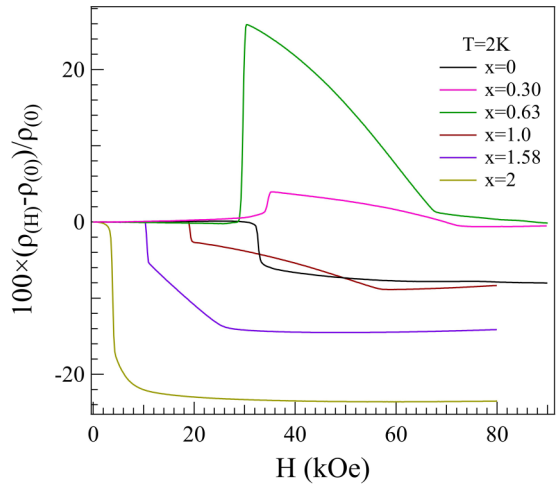

FIG. 5. Magnetoresistance of $MnBi_{2-x}Sb_xTe_4$ at 2 K in fields up to 90 kOe. The measurements were performed with the electrical current in the *ab* plane and magnetic fields along the crystallographic *c* axis. $\rho(H)$ was obtained by averaging the data collected in positive and negative fields. Data for $MnBi_2Te_4$ were replotted from Ref. [14].

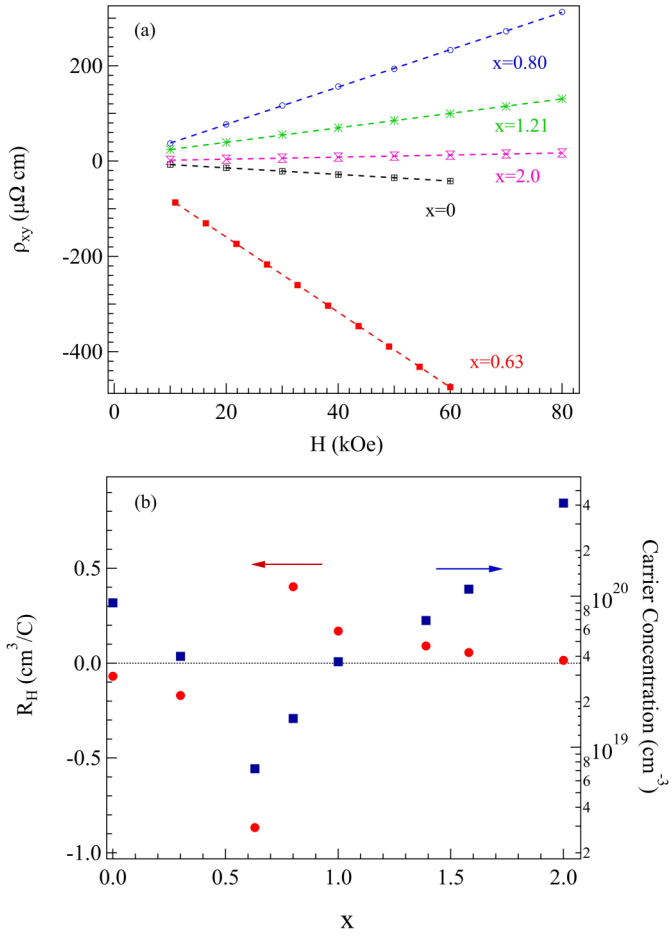

FIG. 6. (a) Field dependence of Hall resistivity of $MnBi_{2-x}Sb_xTe_4$ at room temperature. The measurements were performed with the electrical current in the *ab* plane and magnetic fields along the crystallographic *c* axis. Dashed lines show the linear fitting. (b) The compositional dependence of the Hall coefficient and charge carrier concentration at room temperature. Note that compositions with $x \leqslant 0.63$ are *n* type and a crossover from *n* type to *p* type occurs above $x = 0.63$.

centered at T_N and is suppressed on cooling below T_N, signaling reduced magnetic scattering of electron transport in the magnetically ordered state. In contrast, $\rho(T)$ of $MnSb_2Te_4$ shows a minimum around 50 K, a semiconductinglike temperature dependence below about 50 K, and a slope change at T_N. This temperature dependence suggests that the effect of magnetic order on the electrical resistivity in $MnSb_2Te_4$ is quite different from that in $MnBi_2Te_4$. As presented earlier in Fig. 3, below about 80 K, the H/M of $MnSb_2Te_4$ deviates from the linear temperature dependence. The semiconductinglike temperature dependence of $\rho(T)$ below 50 K seems to result from the short-range magnetic correlations above T_N in $MnSb_2Te_4$. $\rho(T)$ of Sb-rich compositions shows a similar temperature dependence as $MnSb_2Te_4$, but with a more gradual change cooling across T_N, possibly due to the chemical disorder effect. $\rho(T)$ of Bi-rich compositions resembles that of $MnBi_2Te_4$. As discussed later, our DFT calculations suggest that the doped holes have significant Mn 3*d* character, which drives the *p*-type Sb-rich compositions to become more resistive upon cooling across T_N.

Figure 5 shows the magnetoresistance (MR) at 2 K in fields up to 90 kOe. The measurements were performed with the electrical current in the *ab* plane and magnetic fields along the crystallographic *c* axis. $\rho(H)$ was obtained by averaging the data collected in positive and negative fields. $MnBi_2Te_4$ shows a negative MR with a steplike change at $H_{c1} \approx 33$ kOe, where the spin-flop transition occurs, and a slope change around $H_{c2} \approx 78$ kOe, where the magnetic moment saturates. For all doped compositions investigated in this work, the steplike change at H_{c1} and the slope change H_{c2} are observed in the MR curves. Both critical fields become smaller with increasing Sb doping. The critical fields determined from MR curves agree with those determined from magnetic measurements. $MnSb_2Te_4$ shows a negative MR $\approx 23\%$ above 3 kOe, and above this critical field MR shows little field dependence. It is interesting to note that two compositions with $x = 0.30$ and $x = 0.63$ show a positive MR, in contrast to the negative MR of other compositions. As presented later, these two compositions are *n* type from the Hall measurements.

The Hall resistivity, Hall coefficient, and charge carrier concentration at room temperature are shown in Fig. 6. The data suggest a transition between *n* type and *p* type near $x = 0.63$ for our $MnBi_{2-x}Sb_xTe_4$ crystals. Near the point of compensation, the Hall coefficient is not particularly meaningful because both types of carriers contribute. However, the analysis of Hall effect data using a single carrier model should be appropriate away from the point of perfect compensation. For $MnBi_2Te_4$, our data suggest a carrier density around 1.3×10^{20} electrons/cm^3, while for $MnSb_2Te_4$, our data suggest a carrier density of about 5×10^{20} holes/cm^3. A multiband model may capture some of the physics for compositions near the compensation point. However, the room-temperature Hall effect data measured for these crystals revealed linear or nearly linear field dependence, thus precluding the use of a multiband model for even the $x = 0.63$ and 0.80 samples.

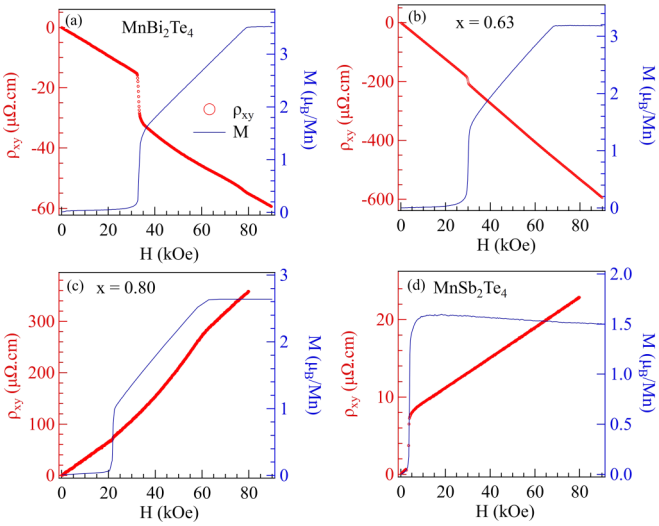

FIG. 7. Hall resistivity of $MnBi_{2-x}Sb_xTe_4$ at 2 K in fields up to 90 kOe. (a) $x = 0$, (b) $x = 0.63$, (c) $x = 0.80$, (d) $x = 2$. The measurements were performed with the electrical current in the *ab* plane and magnetic fields along the crystallographic *c* axis. ρ_{xy} for $MnBi_2Te_4$ was replotted from Ref. [14]. Magnetization data measured with $H//c$ are also plotted.

We measured the field dependence of Hall resistivity at various temperatures for different compositions. Above 50 K, a linear field dependence is always observed for those compositions that are away from the compensation point. The Hall coefficient shows a weak temperature dependence. Upon cooling into the magnetically ordered state, the magnetic field dependence of the Hall resistivity ρ_{xy} changes dramatically and becomes nonlinear. In particular, an anomalous contribution arises after the sharp increase in M associated with the metamagnetic transition. Figure 7 shows the Hall resistivity ρ_{xy} of $MnBi_{2-x}Sb_xTe_4$ at 2 K in fields up to 90 kOe. The measurements were performed with the electrical current in the *ab* plane and magnetic fields along the crystallographic *c* axis. The magnetization data for each composition collected at 2 K and in magnetic fields up to 90 kOe along the *c* axis were also plotted. In Figs. 7(a)–7(c), where a spin-flop transition at H_{c1} is followed by a moment saturation at H_{c2}, a steplike change was observed in ρ_{xy} at H_{c1} and a slope change at H_{c2}. For $MnSb_2Te_4$ [see Fig. 7(d)], a steplike change is observed around 3 kOe in both ρ_{xy} and $M(H)$ curves.

Below the critical field H_{c1}, ρ_{xy} is linear in H, and the Hall coefficient obtained from such data agrees well with those obtained at 300 K. When M is rising linearly towards saturation, as in Figs. 7(a)–7(c), the Hall coefficient is nonlinear due to an increasing anomalous contribution. When the moment reaches a saturation plateau, ρ_{xy} again becomes linear in H. This can be understood as a saturated anomalous contribution and an ordinary Hall coefficient (linear) contribution. Our data suggest that the ordinary Hall coefficient is essentially unchanged by the spin reorientation. However, a large anomalous contribution is observed. For example, an anomalous Hall resistivity of $-20\ \mu\Omega\,\mathrm{cm}$ was observed for $MnBi_2Te_4$ and $+7.3\ \mu\Omega\,\mathrm{cm}$ for $MnSb_2Te_4$. The anomalous Hall contribution can be of either positive or negative sign, and the sign is not immediately apparent based on other physical properties. In $MnBi_{2-x}Sb_xTe_4$ samples, we find that the anomalous contribution has the same sign as the ordinary contribution—a positive anomalous Hall resistivity is observed for hole-doped samples. This may be revealing something rather significant and, if related to an intrinsic anomalous Hall conductivity, could be investigated theoretically from the band structure of the spin-polarized state.

IV. DFT CALCULATIONS

DFT calculations were performed to understand the experimentally observed difference between $MnBi_2Te_4$ and $MnSb_2Te_4$. For each compound, we consider layered antiferromagnetic (AFM) ordering with Mn moments pointing along the $c(a)$ direction, $AFM_{c(a)}$, and ferromagnetic (FM) ordering with Mn moments pointing along the c direction, FM_c. In both compounds, AFM_c is found to be the ground state. This is consistent with the experimental observations for $MnBi_2Te_4$. This can also explain the anisotropic magnetic susceptibility for $MnSb_2Te_4$ shown in Fig. 2, although the magnetic structure needs to be determined experimentally.

The ordered M moment is $\sim 4.2\ \mu_B$ and the total Mn d charge is ~ 4.9 for both compounds. These results are consistent with the valence state of Mn $+2$. By mapping the total energy of this magnetic ordering to that of a Heisenberg-type model consisting of exchange coupling J between Mn moments and the single-ion anisotropy D,

$$H = \sum_{ij} J_{ij}\vec{S}_i \cdot \vec{S}_j - D\sum_i \left|S_i^z\right|^2, \tag{1}$$

$J_cS^2 \sim 1.21$ meV and $DS^2 \sim 0.74$ meV for $MnBi_2Te_4$ and $J_cS^2 \sim 1.18$ meV and $DS^2 \sim 0.45$ meV for $MnSb_2Te_4$. Here, J_c is the nearest-neighbor interlayer coupling, $J_c > 0$ implies it is antiferromagnetic, and $D > 0$ implies uniaxial anisotropy. As far as these properties are considered, the two compounds look nearly identical.

Figure 8 shows the total and partial density of states of $MnBi_2Te_4$ [Fig. 8(a)] and $MnSb_2Te_4$ [Fig. 8(b)]. Our results agree with previous reports [4,13]. Again, the two compounds look very similar, especially Mn $3d$ states appearing at -3 eV from majority spins and 1 eV from minority spins, and Te $5p$ states dominating at the valence-band maximum with some admixture with Mn $3d$ states. While the low-energy part of the conduction band is dominated by Mn $3d$ minority spin states with some admixture with Bi $6p$ or Sb $5p$ states, there is a noticeable difference between $MnBi_2Te_4$ and $MnSb_2Te_4$. Bi $6p$ states have the largest weight at the conduction-band minimum of $MnBi_2Te_4$, while Sb $5p$ states have similar weight with Mn d and Te $5p$ states. This difference is caused by heavier Bi than Sb, by which Bi $6p$ states are relatively lower in energy than Sb $5p$ with respect to Mn $3d$ and Te $5p$ states.

While the difference is quite subtle, $MnBi_2Te_4$ and $MnSb_2Te_4$ are expected to behave differently when doped with electrons; electric transport may not be so sensitive to AFM ordering in $MnBi_2Te_4$ because doped electrons predominantly occupy $6p$ states of Bi, which is spatially separated from Mn. On the other hand, when doped with holes, $MnBi_2Te_4$ and $MnSb_2Te_4$ would behave similarly, i.e., antiferromagnetic ordering would make electric transport

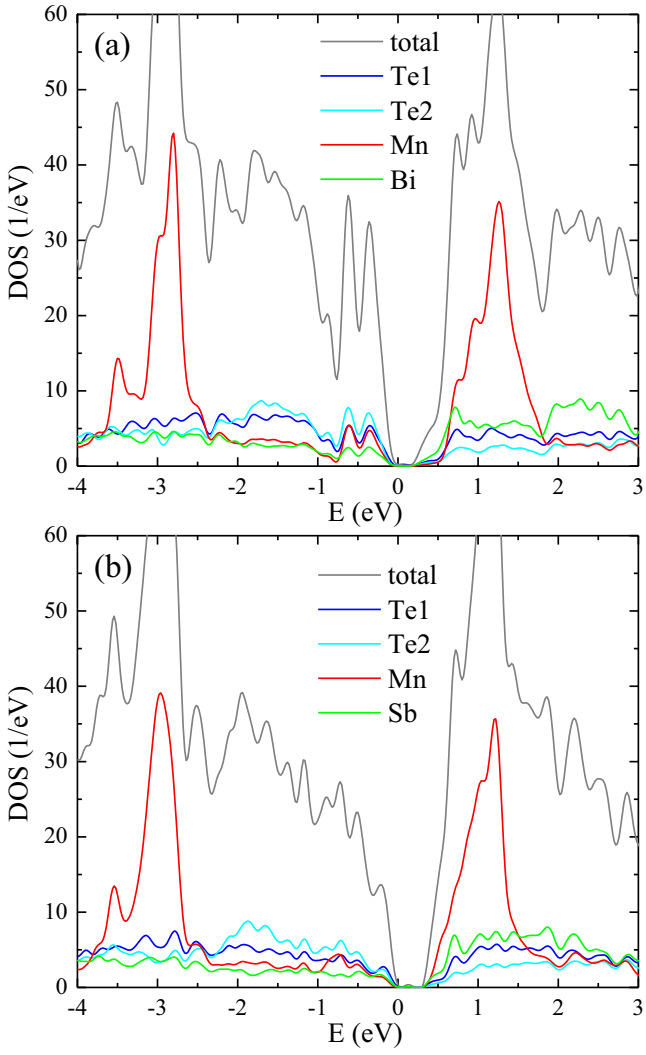

FIG. 8. Density of states (DOS) of (a) $MnBi_2Te_4$ and (b) $MnSb_2Te_4$. Gray lines are the total DOS, other lines are partial DOS; blue is Te1, light blue is Te2, red is Mn, and green is Bi or Sb. Density functional theory calculations include antiferromagnetic ordering with the spin-orbit coupling as described in the text.

more resistive because doped holes have significant Mn $3d$ character.

Within our DFT, the ordered moment on a Mn site remains unchanged, $\sim 4.2\ \mu_B$, between $MnBi_2Te_4$ and $MnSb_2Te_4$. This is consistent with the experimental value of $4.09\ \mu_B$/Mn at 10 K for $MnBi_2Te_4$ [14]. However, the experimental saturation moment shows strong x dependence and is greatly suppressed with increasing Sb doping. This cannot be ascribed to the reduced Mn $3d$ electron density by hole doping. A potential origin of such behavior may be due to the Ruderman-Kittel-Kasuya-Yosida (RKKY) interaction induced by doped holes [23–25]. This could induce magnetic frustrations, resulting in the reduction in the ordered moment, while the effective moment might remain unaffected.

V. DISCUSSION

Previous DFT calculations show that $MnSb_2Te_4$ prefers to crystallize into the same rhombohedral structure as $MnBi_2Te_4$ [13]. However, there are no experimental details about the symmetry and atomic parameters of $MnSb_2Te_4$ reported before. The successful growth of $MnSb_2Te_4$ crystals in this work and our x-ray diffraction studies confirm the DFT predictions and provide experimental data on the lattice parameters and atomic positions. More importantly, the existence of $MnSb_2Te_4$ isostructural to $MnBi_2Te_4$ makes possible the synthesis of $MnBi_{2-x}Sb_xTe_4$ in the whole compositional range. The a-lattice constant, and thus the nearest-neighbor Mn-Mn distance, decreases with increasing Sb content accompanied by the suppression of the Mn-Te-Mn bond angle. Both are expected to modify the magnetic interactions in the hexagonal plane. The direct antiferromagnetic interaction between nearest Mn-Mn neighbors increases with reduced Mn-Mn distance, which competes with the dominant intralayer ferromagnetic interaction and may contribute to the suppressed saturation moment together with the reduced single-ion anisotropy.

Figure 9 summarizes the evolution with Sb content of Neel temperature, effective moment, Weiss constant, saturation moment, and the critical fields. The magnetic field required for the flop transition is labeled as H_{c1} and the larger field to saturate the moment is H_{c2}. The colored bars in Fig. 9(a) were plotted to highlight that the crossover from n-type to p-type conduction occurs around a critical Sb content of $x_c = 0.63$. However, no abrupt change or obvious anomaly around x_c was observed for the other parameters plotted in Fig. 9. This indicates that around the critical composition, the type and concentration of charge carriers can be finely tuned, possibly without inducing any abrupt change of the magnetism.

The effective moments obtained from the Curie-Weiss fitting of H/M curves of different compositions are all around $5.3 \pm 0.1\ \mu_B$/Mn and show no noticeable composition dependence. This effective moment is as expected for a high-spin Mn^{2+} with an electronic configuration of $t_{2g}^3 e_g^2$. The absence of noticeable compositional dependence of μ_{eff} also indicates that there is not a valence or spin state change in $MnBi_{2-x}Sb_xTe_4$.

The Weiss constant for $MnBi_2Te_4$ is 6 K, which is consistent with that reported by Lee *et al.* [6]. With increasing Sb content in $MnBi_{2-x}Sb_xTe_4$, the Weiss constant gradually decreases to -19 K for $MnSb_2Te_4$. It is interesting to note that n-type compositions show a positive Weiss temperature, while the p-type compositions show a negative Weiss temperature. As pointed out by Otrokov *et al.* [2], the temperature-independent χ_0 affects the Curie-Weiss fitting as well as the magnitude of Weiss constant. However, reasonable fitting with χ_0 included also gives a negative Weiss constant for $MnSb_2Te_4$, which suggests the dominant antiferromagnetic interactions in the paramagnetic state of $MnSb_2Te_4$. This is in sharp contrast to the ferromagnetic interactions dominant in $MnBi_2Te_4$ and may have a profound effect on the physical properties. The ferromagnetic fluctuations in $MnBi_2Te_4$ have been proposed to break time-reversal symmetry, inducing the gap opening of surface states. It would be interesting to check whether such a gap opening of surface states also occurs in $MnSb_2Te_4$ below and above T_N.

The saturation moments at 2 K of different compositions are summarized in Fig. 9(d). The saturation moment is drastically suppressed by the replacement of Bi by Sb. At

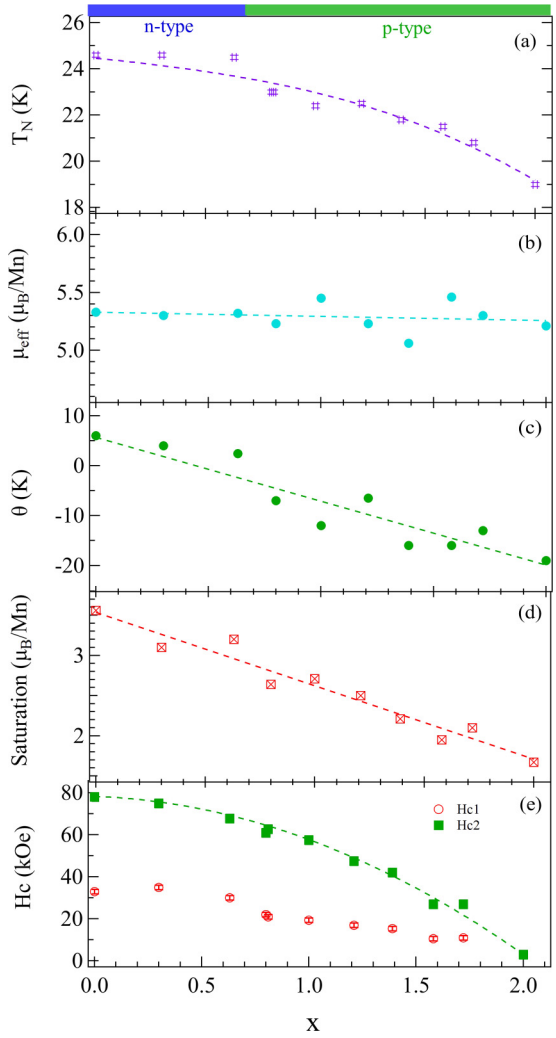

FIG. 9. The compositional dependence of (a) Neel temperature, (b) effective moment obtained from the Curie-Weiss fitting of H/M curves, (c) Weiss constant obtained from the Curie-Weiss fitting of H/M curves, (d) saturation moment at 2 K, and (e) critical magnetic fields for spin flop, H_{c1}, and moment saturation, H_{c2}, determined from magnetic and transport measurements. The dashed curves/lines are a guide for the eye.

2 K, a saturation moment of 3.56 μ_B/Mn was observed for $MnBi_2Te_4$. Surprisingly, a much smaller saturation moment of 1.67 μ_B/Mn was observed for $MnSb_2Te_4$. The saturation moment decreases linearly with increasing Sb content. For high-spin Mn^{2+} with an electronic configuration of $t_{2g}^3e_g^2$, a saturation moment of 5 μ_B/Mn is expected. It is worth mentioning that our x-ray powder diffraction found only a few percent of Sb_2Te_3 likely from the residual flux on the crystals. This amount of nonmagnetic impurity is not enough to induce such a large reduction of saturation moment. We further measured magnetization at 2 K in magnetic fields up to 120 kOe without finding any other field-induced changes. In magnetic fields above H_{c2}, the magnetization shows little field dependence up to 120 kOe. We also measured M/H of $MnSb_2Te_4$ in a field of 50 kOe and M/H tends to saturate below 5 K. All these suggest that the suppression of the saturation moment in Sb-bearing compositions is an intrinsic behavior, though the magnetic structure should be verified to exclude more complex spin structures causing the apparent difference in saturation moment.

Our x-ray diffraction (see Fig. 1) shows that the Mn-Te bond length has little doping dependence, which implies little change in the Mn-Te bond covalency. However, the nearest-neighbor Mn-Mn distance is reduced with increasing Sb content. It is expected that the enhanced direct antiferromagnetic interactions would compete with the dominant nearest-neighbor ferromagnetic interaction. Therefore, the reduced saturation moment can result from the magnetic fluctuations in the magnetically ordered state. If this scenario is right, we would expect the ordered moment of $MnSb_2Te_4$ is also smaller than that of $MnBi_2Te_4$. Neutron diffraction is needed to investigate the magnetic structure and ordered moment in $MnSb_2Te_4$ and maybe the evolution with Sb doping, especially if $MnSb_2Te_4$ has a different magnetic structure other than the simple A-type antiferromagnetism observed in $MnBi_2Te_4$. On the other hand, it would be interesting to investigate the magnetization in much higher magnetic fields for possible field-induced transitions. This is especially true for $MnSb_2Te_4$ with such a small saturation moment.

Figure 9(e) shows the critical magnetic fields for spin flop, H_{c1}, and moment saturation, H_{c2}, determined from magnetic and transport measurements with magnetic fields applied along the crystallographic c axis. Both critical fields decrease with increasing Sb content. For $MnSb_2Te_4$, a magnetic field as small as 3 kOe is enough to saturate the magnetization. For a uniaxial antiferromagnet, the spin-flop field and saturation field can be written in terms of the interlayer antiferromagnetic exchange (J_c) and single-ion anisotropy (D) as $g\mu_B H_{c1} = 2SD\sqrt{zJ_c/D - 1}$ and $g\mu_B H_{c2} = 2SD(zJ_c/D - 1)$, respectively, where $g = 2$, $z = 6$ is the coordination number for Mn to other Mn in layers above and below. Therefore, J_c and D can be calculated as $SD = (1/2)g\mu_B H_{c1}(H_{c1}/H_{c2})$, and $SJ_c = \frac{1}{2z}g\mu_B H_{c2}[(H_{c1}/H_{c2})^2 + 1]$, respectively. The calculated SD and SJ_c are plotted in Fig. 10. For $MnSb_2Te_4$ with

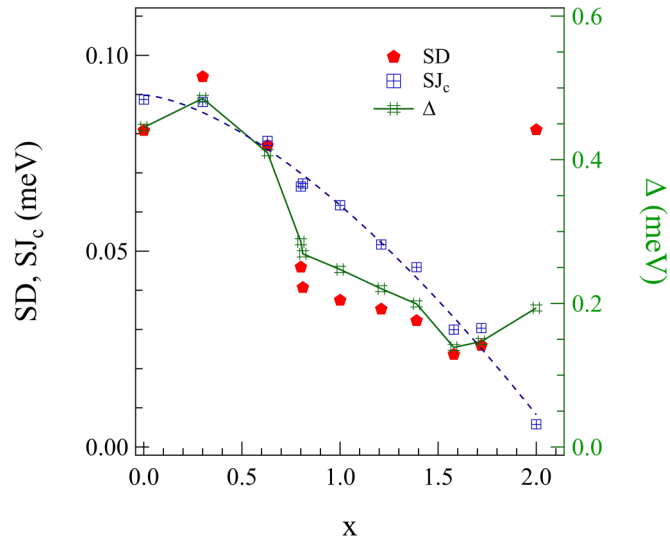

FIG. 10. Compositional dependence of single-ion anisotropy, SD, and interlayer magnetic interaction, SJ_c, and spin gap, △. The solid and dashed curves are a guide to the eye.

only a spin-flip transition at a field of H_c, $SJ_c = g\mu_B H_c/z$. SD of $MnSb_2Te_4$ can be estimated as $SD = (1/2)g\mu_B H_c^* - zSJ_c$, where H_c^* is the critical field applied perpendicular to the c axis to saturate the magnetic moment.

Both SD and SJ_c decrease with increasing Sb content for $x \leqslant 1.72$, although they show distinct compositional dependence. It is interesting to note that SJ_c decreases monotonically with increasing Sb content, although the c lattice shows little doping dependence. The steplike change of SD around $x = 0.70$ signals two different compositional dependences of SD: Below $x = 0.63$, SD shows little doping dependence; for $0.80 \leqslant x \leqslant 1.72$, SD decreases monotonically with increasing Sb content. This corresponds with the change in carrier type and more compositions will be studied to reveal the details of the doping dependence of SD in the composition range $0.63 < x < 0.80$.

In the Sb-rich composition around $x = 1.72$, SD and SJ_c are comparable to each other. For $MnSb_2Te_4$, magnetization saturates in a field of 3 kOe at 2 K. The critical composition where the spin-flop transition disappears is in $1.72 < x \leqslant 2$. Above $x = 1.72$, SJ_c/SD is smaller than $2/z$ required for the spin-flop transition and, therefore, magnetization saturates directly with increasing field. As shown in Fig. 10, SD is one order of magnitude larger than SJ_c for $MnSb_2Te_4$. The magnitude of interlayer coupling relative to the single-ion anisotropy determines the different magnetic properties between $MnSb_2Te_4$ and $MnBi_2Te_4$. We noticed that for $MnSb_2Te_4$, the SJ_c and SD estimated here are different from our DFT calculations. This indicates that Sb doping has a complex effect on the magnetic interactions and/or that the magnetic structure of $MnSb_2Te_4$ may not be a simple A-type antiferromagnetism.

The spin gap can be calculated as $\triangle = 2SD\sqrt{zSJ_c/SD + 1}$. Figure 10 also shows the doping dependence of the spin gap. The spin gap in $MnBi_2Te_4$ is about 0.45 meV and it decreases with increasing Sb content to about 0.15 meV for $x = 1.72$. Above $x = 1.72$, the spin gap slightly increases to 0.20 meV for $MnSb_2Te_4$. These need to be confirmed experimentally by, for example, inelastic neutron scattering.

With the knowledge of SD and SJ_c, the magnetic field required to saturate magnetization when the field is applied perpendicular to the c axis can be calculated as $g\mu_B H_c^* = 2(zSJ_c + SD)$. As shown in Fig. 11, the calculated and measured critical fields agree well for all compositions.

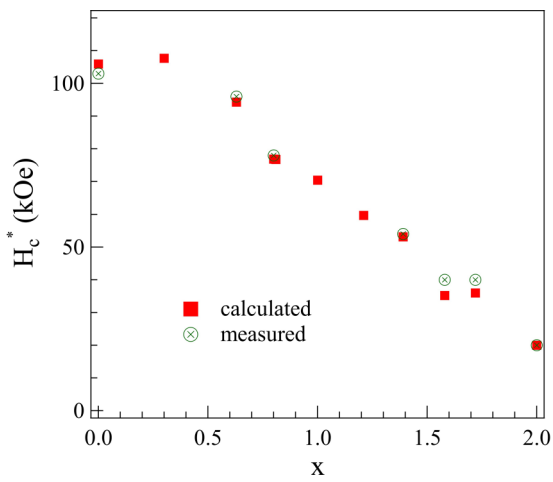

FIG. 11. The critical magnetic fields required to saturate magnetization when the field is applied perpendicular to the crystallographic c axis. The calculated values are obtained using experimental results to obtain $g\mu_B H_c^* = 2(zSJ_c + SD)$.

VI. SUMMARY

In summary, we study the evolution of structural, magnetic, and transport properties in the whole compositional range of $MnBi_{2-x}Sb_xTe_4$. Our results show close correlation between the structural, magnetic, and transport properties in this system. With increasing Sb content, the lattice parameters, the antiferromagnetic ordering temperature, Weiss constant, saturation moment at 2 K, the critical fields for spin-flop transition, and moment saturation decrease. Data analyses suggest that the interlayer exchange coupling, single-ion anisotropy, and magnon gap also decrease with the substitution of Bi by Sb. The significant reduction in the saturation moment at 2 K cannot be explained simply by the different Mn-Te bond covalency. Instead, the enhanced direct interactions in the *ab* plane due to the reduced Mn-Mn bond length and also the RKKY interactions induced by doped holes should be considered. The modified in-plane magnetic interactions, together with reduced interlayer coupling and single-ion anisotropy with Sb doping, might induce strong magnetic fluctuations even in the magnetically ordered state if the same A-type antiferromagnetic structure is maintained for the whole system. All these need to be further investigated with advanced techniques such as neutron scattering.

Near $x_c = 0.63$, a transition from n-type to p-type conduction is observed in our crystals. Further careful optimization of growth parameters and fine tuning of the chemical compositions are needed to control the magnetism, the number of lattice defects, charge carrier concentration, and mobility to facilitate the realization of theoretically predicted topological properties.

The U.S. Department of Energy will provide public access to these results of federally sponsored research in accordance with the U.S. DOE Public Access Plan [26].

ACKNOWLEDGMENTS

This work was supported by the U.S. Department of Energy, Office of Science, Basic Energy Sciences, Materials Sciences and Engineering Division. Ames Laboratory is operated for the U.S. Department of Energy by Iowa State University under Contract No. DE-AC02-07CH11358. This manuscript has been co-authored by employees of UT-Battelle, LLC under Contract No. DE-AC0500OR22725 with the U.S. Department of Energy. The United States Government retains and the publisher, by accepting the article for publication, acknowledges that the United States Government retains a nonexclusive, paid-up, irrevocable, worldwide license to publish or reproduce the published form of this manuscript, or allow others to do so, for the United States Government purposes.

[1] M. M. Otrokov, T. V. Menshchikova, M. G. Vergniory, I. P. Rusinov, A. Y. Vyazovskaya, Y. M. Koroteev, G. Bihlmayer, A. Ernst, P. M. Echenique, A. Arnau *et al.*, 2D Mater. **4**, 025082 (2017).
[2] M. M. Otrokov, I. I. Klimovskikh, H. Bentmann, A. Zeugner, Z. S. Aliev, S. Gass, A. U. Wolter, A. V. Koroleva, D. Estyunin, A. M. Shikin *et al.*, arXiv:1809.07389.
[3] D. Zhang, M. Shi, K. He, D. Xing, H. Zhang, and J. Wang, Phys. Rev. Lett. **122**, 206401 (2019).
[4] B. Chen, F. Fei, D. Zhang, B. Zhang, W. Liu, S. Zhang, P. Wang, B. Wei, Y. Zhang, J. Guo *et al.*, arXiv:1903.09934.
[5] M. M. Otrokov, I. P. Rusinov, M. Blanco-Rey, M. Hoffmann, A. Y. Vyazovskaya, S. V. Eremeev, A. Ernst, P. M. Echenique, A. Arnau, and E. V. Chulkov, Phys. Rev. Lett. **122**, 107202 (2019).
[6] S. H. Lee, Y. Zhu, Y. Wang, L. Miao, T. Pillsbury, S. Kempinger, D. Graf, N. Alem, C.-Z. Chang, N. Samarth *et al.*, arXiv:1812.00339.
[7] J. Li, Y. Li, S. Du, Z. Wang, B. Gu, S. Zhang, K. He, W. Duan, and Y. Xu, Sci. Adv. **5**, eaaw5685 (2019).
[8] R. Vidal, H. Bentmann, T. Peixoto, A. Zeugner, S. Moser, C. Min, S. Schatz, K. Kissner, M. Ünzelmann, C. Fornari *et al.*, arXiv:1903.11826.
[9] Y. Gong, J. Guo, J. Li, K. Zhu, M. Liao, X. Liu, Q. Zhang, L. Gu, L. Tang, X. Feng *et al.*, Chin. Phys. Lett. **36**, 076801 (2019).
[10] J. Cui, M. Shi, H. Wang, F. Yu, T. Wu, X. Luo, J. Ying, and X. Chen, Phys. Rev. B **99**, 155125 (2019).
[11] Y. Deng, Y. Yu, M. Z. Shi, J. Wang, X. H. Chen, and Y. Zhang, arXiv:1904.11468.
[12] D. S. Lee, T.-H. Kim, C.-H. Park, C.-Y. Chung, Y. S. Lim, W.-S. Seo, and H.-H. Park, CrystEngComm **15**, 5532 (2013).
[13] S. Eremeev, M. Otrokov, and E. V. Chulkov, J. Alloys Compd. **709**, 172 (2017).
[14] J.-Q. Yan, Q. Zhang, T. Heitmann, Z. Huang, W. Wu, D. Vaknin, B. Sales, and R. McQueeney, Phys. Rev. Mater. **3**, 064202 (2019).
[15] C. Liu, Y. Wang, H. Li, Y. Wu, Y. Li, J. Li, K. He, Y. Xu, J. Zhang, and Y. Wang, arXiv:1905.00715.
[16] A. Zeugner, F. Nietschke, A. U. Wolter, S. Gaß, R. C. Vidal, T. R. Peixoto, D. Pohl, C. Damm, A. Lubk, R. Hentrich *et al.*, Chem. Mater. **31**, 2795 (2019).
[17] C.-Z. Chang, J. Zhang, X. Feng, J. Shen, Z. Zhang, M. Guo, K. Li, Y. Ou, P. Wei, L.-L. Wang *et al.*, Science **340**, 167 (2013).
[18] M. A. McGuire, Q. Zheng, J. Yan, and B. C. Sales, Phys. Rev. B **99**, 214402 (2019).
[19] G. Kresse and J. Furthmüller, Phys. Rev. B **54**, 11169 (1996).
[20] G. Kresse and D. Joubert, Phys. Rev. B **59**, 1758 (1999).
[21] J. P. Perdew, K. Burke, and M. Ernzerhof, Phys. Rev. Lett. **77**, 3865 (1996).
[22] Z. S. Aliev, I. R. Amiraslanov, D. I. Nasonova, A. V. Shevelkov, N. A. Abdullayev, Z. A. Jahangirli, E. N. Orujlu, M. M. Otrokov, N. T. Mamedov, M. B. Babanly *et al.*, J. Alloys Compd. **789**, 443 (2019).
[23] M. A. Ruderman and C. Kittel, Phys. Rev. **96**, 99 (1954).
[24] T. Kasuya, Prog. Theor. Phys. **16**, 45 (1956).
[25] K. Yosida, Phys. Rev. **106**, 893 (1957).
[26] http://energy.gov/downloads/doe-public-access-plan